

Evolution of Shell Structure at $N = 32$ and 34 : Insights from Realistic Nuclear Forces and the Role of Tensor Component

Subhrajit Sahoo, Praveen C. Srivastava

^aDepartment of Physics Indian Institute of Technology Roorkee, Roorkee, 247667, Uttarakhand, India

Abstract

The evolution of nuclear shell structures at $N = 32$ and 34 are studied in nuclei far from the stability line using effective interactions derived from realistic nuclear forces. The state-of-the-art *ab initio* in-medium similarity renormalization group method is used for this purpose. The calculated results are consistent with experimental observations, and predictions are made where experimental data are unavailable. The shell gaps are analyzed from the evolution of effective single-particle energies, and various facets of nuclear interaction, such as central, spin-orbit, and tensor parts, are addressed by spin-tensor decomposition of the effective interactions. The roles played by these components in the development of shell closure, particularly by the tensor components, were highlighted throughout the study. Then, we discussed the low-lying structure of the exotic $N = 32$ isotones below Ca. The present work demonstrates essential components of nuclear force in shaping magic numbers far from stability and provides deeper insights into the structure of exotic nuclei.

Keywords: *Ab initio*, Shell evolution, Spin-tensor decomposition, Tensor component, $N = 32$ and 34 isotones

1. Introduction

The nuclei, characterized by large N/Z ratios, are often referred to as exotic nuclei and challenge the traditional understanding of nuclear shell structure. The canonical magic numbers such as $N = 8, 20, 28, 40$, and 50 , which are believed to be immutable, tend to diminish or vanish, and new magic numbers like $N = 14, 16, 32$, and 34 emerge in the exotic systems [1, 2]. In the past years, the appearance of new magic numbers $N = 32$ and 34 in the vicinity of doubly magic ^{48}Ca has been a major focus for both experimental and theoretical nuclear physicists [2, 3, 4, 5, 6, 7, 8, 9, 10, 11, 12, 13, 14]. The experimental studies establish $N = 32$ sub-shell closure in neutron-rich Ti to Ca isotopes and the onset of a new shell gap at $N = 34$ in Ca [6, 7, 8, 9]. Additionally, further investigations revealed the persistence of the $N = 34$ sub-shell gap in Ar, extending even below Ca [14]. This region of the Segrè chart provides valuable inputs for understanding the shell evolution and nature of nuclear interactions away from the stability line.

The magicity at $N = 32$ and $N = 34$ in Ca isotopes was first predicted by Otsuka *et al.*, as a consequence of strong, attractive tensor force between protons and neutrons occupying the $\pi f_{7/2}$ and $\nu f_{5/2}$ single-particle orbitals, respectively [15]. The shell structure in this region was extensively studied from various effective interactions that support the appearance of a new magic number at $N = 34$ in Ca [16, 17, 18, 19, 20, 21, 22]. This was later confirmed by Steppenbeck *et al.* through measurements of the 2^+ excitation energy in ^{54}Ca [6]. Further, the spin-tensor decomposition of the effective interactions reveals that, in addition

to the tensor component, the central part also makes essential contributions in building the $N = 34$ shell gap [2, 23]. However, most of these studies are based on phenomenological interactions where the nucleon-nucleon matrix elements of the effective interactions were adjusted empirically. The spin-tensor analysis performed for effective interactions of microscopic origin in Ref. [24] fell short in capturing accurate shell evolution, primarily due to the absence of three-body forces. The knowledge of different components of microscopic nucleon-nucleon interactions and their impact on forming magic numbers in exotic systems is still limited.

The fundamental interest of the nuclear theory group lies in explaining the structure of nuclei from the underlying nuclear forces [25, 26, 27]. Recent advances in *ab initio* theory have enabled the nonperturbative decoupling of effective interactions or Hamiltonians from realistic NN and NNN nucleon potentials through various *ab initio* approaches like No Core Shell Model (NCSM) [28, 29], Coupled Cluster Theory (CC) [30, 31], and In Medium Similarity Renormalization Group (IMSRG) [32, 33, 34]. While NCSM is limited to lower mass nuclei [35, 36], the applicability of CC [37, 38] and IMSRG [39, 40, 41, 42] methods has been extended to medium- and heavier-mass regions. With such advancement, it is essential to address the evolution of shell structure from the underlying two- and three-nucleon forces. A thorough understanding of the microscopic origins behind the emergence of new magic numbers is needed. Moreover, with advancements in experimental facilities, the study of exotic isotopes has become a central focus. This progress makes simultaneous theoretical investigations into the structural properties of exotic nuclei highly desirable.

The valance-space effective interactions, derived from QCD-

Email addresses: s_sahoo@ph.iitr.ac.in (Subhrajit Sahoo), praveen.srivastava@ph.iitr.ac.in (Praveen C. Srivastava)

based chiral NN and NNN potentials using the state-of-the-art IMSRG method (VS-IMSRG), have shown promising results in describing the binding energies, spectroscopy of low-lying states, collectivity, and electromagnetic observables of both closed- and open-shell nuclei [33, 34, 36, 40]. The breaking of conventional shell gaps at $N = 20, 28$ and the appearance of new magic numbers at $N = 14$ have been well explained within VS-IMSRG framework [39, 43, 44].

In this letter, we have investigated the shell closures at $N = 32$ and 34 by studying a series of isotopes and isotones around the doubly magic ^{48}Ca employing VS-IMSRG interactions. Shell features, such as the excitation energy of the first 2^+ states, are calculated and compared with available experimental data. The shell gaps are discussed from the evolution of single-particle energies, and a spin-tensor decomposition is performed to elucidate the roles of the central, spin-orbit, and tensor parts in the development of shell gaps. Then, we presented the low-lying structures of the exotic $N = 32$ isotones below Ca, which are of current experimental interest [11, 12, 13, 14]. Their low-energy excited states, $E2$ transitions, quadrupole moments, and occupation numbers are studied in detail. The paper is structured as follows: we begin with a brief overview of the IMSRG formalism and outline the calculation details in Sec. 2. All the *ab initio* results and their interpretations are presented in Sec. 3, followed by a short summary of the work in Sec. 4.

2. Method

In the IMSRG approach, we start from the intrinsic A -body Hamiltonian given by

$$H = \frac{1}{A} \sum_{i < j}^A \frac{(\vec{p}_i - \vec{p}_j)^2}{2m} + \sum_{i < j}^A V_{ij}^{NN} + \sum_{i < j < k}^A V_{ijk}^{NNN}, \quad (1)$$

where \vec{p} is nucleon momentum in laboratory frame, m represents the nucleon mass, V_{ij}^{NN} and V_{ijk}^{NNN} correspond to NN and NNN nuclear forces, respectively. The well-established chiral two- and three-body nuclear forces EM1.8/2.0 interaction [45, 46], comprising of a next-to-next-to-next-to-leading order ($N^3\text{LO}$) NN potential evolved through Similarity Renormalization Group (SRG) to momentum resolution scale $\lambda=1.8 \text{ fm}^{-1}$ and a NNN force at next-to-next-to-leading order ($N^2\text{LO}$) with momentum cutoff $\Lambda=2.0 \text{ fm}^{-1}$, has been used for this purpose. In practice, the Hamiltonian is written in terms of creation (a_i^\dagger) and annihilation (a_i) operators as;

$$H = E_0 + \sum_{ij} f_{ij} \{a_i^\dagger a_j\} + \frac{1}{4} \sum_{ijkl} \Gamma_{ijkl} \{a_i^\dagger a_j^\dagger a_l a_k\} + \frac{1}{36} \sum_{ijklmn} W_{ijklmn} \{a_i^\dagger a_j^\dagger a_k^\dagger a_n a_m a_l\}. \quad (2)$$

Here E_0 , f , Γ , and W correspond to zero-, one-, two- and three-body operators, respectively, and are normal ordered with respect to a Hartree-Fock or ensemble reference state [33, 34].

In the VS-IMSRG framework, an effective Hamiltonian is decoupled from the large Hilbert space for a chosen valance

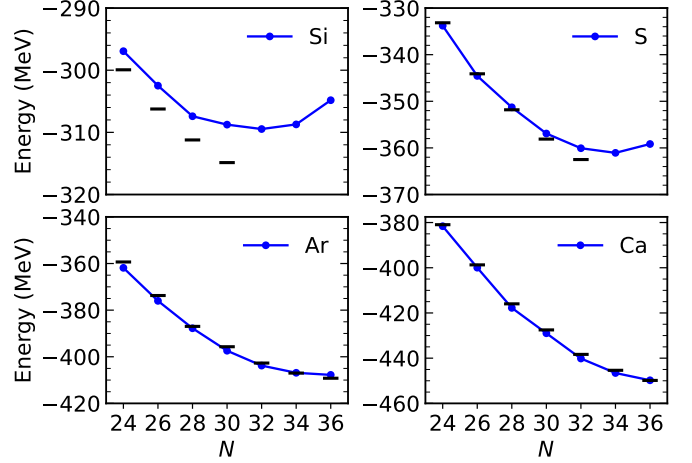


Figure 1: Calculated (blue) and experimental (black) [52] ground state binding energies of nuclei with $Z \leq 20$.

space that contains the necessary degrees of freedom to describe the low-lying states in nuclei of interest. This is achieved by applying a continuous sequence of unitary transformations or evolving the Hamiltonian through the flow equation given by;

$$\frac{dH(s)}{ds} = [\eta(s), H(s)], \quad (3)$$

where ‘ s ’ is called the flow parameter and $\eta(s) = \frac{dU(s)}{ds} U^\dagger(s)$ is known as the anti-hermitian generator that performs the required unitary transformation. The contributions of NNN forces are well captured up to the two-body level due to normal ordering. Hence, in practical calculations, the Hamiltonian (Eq. (2)) is truncated at the two-body level in the IMSRG evolution to overcome computational and numerical challenges (known as IMSRG(2) approximation), and Magnus formalism [47] is used to solve Eq. (3).

The IMSRG calculations are carried out in harmonic oscillator basis at $\hbar\omega=16 \text{ MeV}$ with $e = 2n + l \leq e_{max} = 12$, and additional truncation on NNN forces $e_1 + e_2 + e_3 \leq E_{3max} = 24$, large enough to reach convergence [48]. In this work, the VS-IMSRG interactions are decoupled for fp -shell for both protons and neutrons above ^{40}Ca core for nuclei with $Z \geq 20$. For neutron-rich nuclei with $Z < 20$, our valance space spans protons in sd -shell and neutrons in fp shell above a ^{28}O core within which the properties of neutron-rich nuclei are well reproduced in earlier IMSRG works [40, 41]. The effective Hamiltonians and consistently evolved effective $E2$ operators for the chosen valance space are generated through IMSRG calculations performed using the IMSRG++ [49] code of Ref. [34]. The valance-space effective Hamiltonians are diagonalized, and the corresponding transition densities are obtained through KSHELL code [50].

3. Results and Discussion

The sub-shell gaps at $N = 32$ and 34 are investigated in neutron-rich isotopes with $16 \leq Z \leq 26$. Since these isotopes, particularly those with $Z < 20$, lie on the extreme neutron-rich

side and in medium mass regions, it is important to track the neutron drip line as well as the convergence of *ab initio* calculations with *NNN* forces. The VS-IMSRG results, calculated with $E_{3max} = 14$, show good convergence behavior in nuclei with $A \sim 40$ in Ref. [39] while those for nuclei with $A \sim 45$ have small differences [40]. The authors in Ref. [40] also do not guarantee convergence in heavier nuclei with this E_{3max} truncation. To ensure convergence in our calculation, we have reported the excitation energies of low-lying states in ^{60}Fe obtained from two sets of IMSRG calculations; $e_{max} = 12$, $E_{3max} = 22$ and $e_{max} = 12$, $E_{3max} = 24$ in Table 1. The identical excitation energies across both sets imply that $E_{3max} = 24$ truncation is sufficient enough to achieve proper convergence.

Table 1: Excitation energies (in MeV) of the low-lying spectra of ^{60}Fe calculated with different sets of e_{max} , E_{3max} .

States(J^π)	e_{max} , E_{3max}	
	(12,22)	(12,24)
0_1^+	0.000	0.000
2_1^+	1.000	1.000
0_2^+	2.360	2.360
4_1^+	2.625	2.626
2_2^+	3.017	3.016
4_2^+	3.743	3.744

Then, the ground state (g.s.) binding energies in the isotopic chains of nuclei having extreme N/Z ratios or for those with $Z \leq 20$ are shown in Fig. 1 to locate the neutron drip line within these chains. The g.s. energies are well reproduced in the Ca, Ar, and S isotopic chains while they suffer underestimation of around ~ 4 MeV in neutron-rich Si isotopes. This is consistent with the global survey conducted by Stroberg *et al.* [51] essentially for all nuclei in the range $Z = 2$ to 26 using EM1.8/2.0 interaction, which reports a root-mean-square (rms) deviation of approximately 3.3 MeV from absolute binding energies. The g.s. binding energy trends in Si and S isotopic chains (upper panel of Fig. 1) suggest their corresponding drip lines at $N = 32$ and $N = 34$, respectively. So, in the following sections, we have confined our discussions on Si and S isotopes up to their drip line nucleus.

The energy trends of the first 2^+ excited states ($E(2_1^+)$) in even-even nuclei along an isotopic chain serve as stringent probes to identify shell or sub-shell gaps. The energies of the 2_1^+ states obtained from VS-IMSRG calculations for $20 \leq Z \leq 26$ and $14 \leq Z \leq 20$ isotopes are plotted against their corresponding experimental data in the left and right panel of Fig. 2, respectively. The calculated $E(2_1^+)$ are found at relatively higher energies than their experimental counterparts. Similar results are also observed in earlier IMSRG works [39, 43, 44], and is possibly caused by the IMSRG(2) approximation where the induced three- and higher body forces are ignored. But, the systematic behaviors of the 2_1^+ states are well reproduced from VS-IMSRG calculations. In the left panel of Fig. 2, the relatively high $E(2_1^+)$ at $N = 32$ indicates the presence of $N = 32$ sub-shell gap in Ca and Ti, which weakens in Cr and gradually vanishes at Fe. The energy patterns of the 2_1^+ state show

no signs of $N = 34$ sub-shell closure in Fe to Ti, which appears only in the Ca chain. The spectroscopic studies on *fp*-shell nuclei from nuclear potentials based on chiral perturbation theory also suggest the same conclusion [53]. In *fp*-shell, the $N = 34$ sub-shell gap is an exclusive feature of the Ca chain that sets at Sc [9]. From the right panel of Fig. 2, the $E(2_1^+)$ systematics point towards the persistence of this $N = 34$ sub-shell gap in Ar and S, while the $N = 32$ sub-shell closure is weak or does not extend below Ca. Additionally, the $N = 28$ shell gap remains intact in all isotopes except Si.

The effective (spherical) single-particle energies (ESPEs) of shell model orbits serve as a useful theoretical tool for studying nuclear shell structure. Despite being non-observables, they provide a robust qualitative picture of the evolution of shell gaps in nuclei. The ESPE of an orbit corresponds to the average effects exerted by other nucleons on a nucleon occupying that particular single-particle orbit. In general, assuming the filling of nucleons in normal configuration, the ESPE (ϵ) of an orbit j is evaluated from the angular momentum averaged monopole components ($V_{jj'}^{mon.}$) of the effective Hamiltonian as follows;

$$\text{ESPE}(\epsilon_j) = \epsilon_{0j} + \sum_j V_{jj'}^{mon.} n_{j'}, \quad (4)$$

where ϵ_0 is the bare single-particle energy, and the sum runs over valence-space orbitals j' , $n_{j'}$ being the number of particles in j' . Indeed, the evolution of ESPEs, studied from various phenomenological interactions [15, 16, 23, 20, 22] and effective Hamiltonians derived from realistic nuclear forces [24, 29, 53], has successfully explained the evolution of $N = 14, 16, 20$ and 28 shell gaps. In the present work, we have followed the same formalism to calculate ESPEs from VS-IMSRG interactions and studied the shell evolution by analyzing the energy gaps between relevant orbits in ESPEs. In the subsequent sections, we will see that the calculated ESPEs lead to conclusions similar to those drawn from other popular phenomenological interactions, and their interpretations closely align with the experimental findings. However, we mention that there are also other approaches [54, 55, 56] that aim to calculate ESPEs in a more fundamental way within the context of strongly correlated many-nucleon systems.

The ESPEs of neutron orbitals relative to the lowest $\nu f_{7/2}$ are shown for Fe to Ca in Fig. 3. It can be noted that the neutron ESPEs at $N = 32$ isotones exhibit exactly similar patterns as those observed at $N = 34$ with very small differences in their values. This implies that the effect of neutron-neutron monopole interaction is minor (also observed from phenomenological studies in Ref. [2]), and hence, the interpretations made about shell gaps at $N = 34$ can be extended to those isotopes at $N = 32$. So, in the following sections, we will discuss the shell closures at $N = 32$ and at $N = 34$ from the ESPEs of $N = 34$ isotones. From Fig. 3, we can see that the $N = 32$ sub-shell gap in Fe is disrupted by the presence of $f_{5/2}$ orbital in between $p_{3/2}$ and $p_{1/2}$. This $f_{5/2}$ orbital rises above $p_{1/2}$ and opens up the $N = 32$ sub-shell gap in Cr. As we move to Ti and Ca, the energy gap between $p_{3/2}$ and $p_{1/2}$ increases moderately, reinforcing the $N = 32$ sub-shell gap. On the other

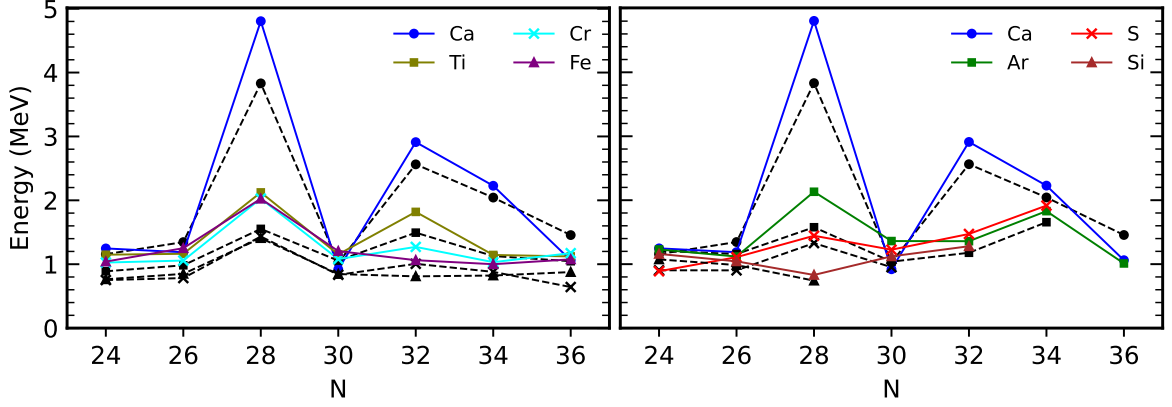


Figure 2: Calculated (colored solid lines) and experimental [52] (black dotted lines) excitation energies of 2_1^+ state in $20 \leq Z \leq 26$ (left) and $14 \leq Z \leq 20$ (right) isotopes.

side, the energy gap between $p_{1/2}$ and $f_{5/2}$ grows significantly from Cr to Ca, becoming large enough in Ca to establish the $N = 34$ sub-shell closure. The $f_{5/2}$ orbital played an important role in building the $N = 32$ and 34 sub-shell gaps. Otsuka *et al.* [15] explained the behavior of $f_{5/2}$ orbital through the strong, attractive tensor force acting between proton-neutron spin-orbit partner ($\pi f_{7/2}$ and $\nu f_{5/2}$) within one major shell. As protons are removed from $\pi f_{7/2}$ orbital (from Fe to Ca), the strength of this force decreases, which leads to an upward shift of $\nu f_{5/2}$ orbital, creating the $N = 32$ and 34 sub-shell gaps.

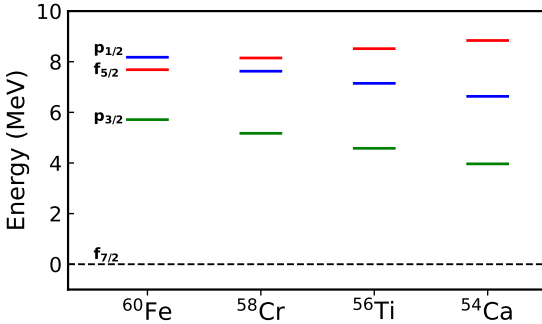


Figure 3: Neutron ESPEs of $N = 34$ isotones in fp -shell.

To understand different components of nuclear force like central, spin-orbit, and tensor parts and their involvement in developing the shell gaps, we have performed spin-tensor decomposition of VS-IMSRG interactions following Refs. [23, 57, 58, 59]. The two-body interactions or two-body matrix elements (tbmes) of the effective interactions can be expressed as

$$V(1, 2) = V = \sum_k U^{(k)} \cdot C^{(k)} = \sum_{k=0,1,2} V^k, \quad (5)$$

where $C^{(k)}$ and $U^{(k)}$ are rank k -tensors in spin and configuration space, respectively. Here, the central, spin-orbit (symmetric and antisymmetric), and tensor components of the matrix element are denoted by V^k corresponding to ranks $k = 0, 1$, and 2 , respectively. The components V^k are calculated from V as

follows [59]

$$\begin{aligned} \langle (ab)LSJT|V^k|(cd)L'S'JT \rangle &= (2k+1) \begin{Bmatrix} L & S & J \\ S' & L' & k \end{Bmatrix} \times \\ &\sum_{J'} (-1)^{J'+k} (2J'+1) \begin{Bmatrix} L & S & J' \\ S' & L' & k \end{Bmatrix} \\ &\times \langle (ab)LSJ'T|V|(cd)L'S'J'T \rangle, \quad (6) \end{aligned}$$

by transforming the normalized and antisymmetrized tbmes from the jj coupled scheme to the LS coupled scheme in the standard way. Then, these LS coupled matrix elements of V^k can be related back to jj coupled matrix elements for further use (for details, see Refs. [57, 58, 59]). Next, we have studied the contribution and roles played by different components of effective interaction in the evolution of ESPEs or in the development of shell structures.

The effect of central, tensor, and spin-orbit components on neutron ESPEs of ^{60}Fe is illustrated in Fig. 4(a). We can see that it is the tensor component of effective interaction that brings down the $f_{5/2}$ orbital to a position between $p_{1/2}$ and $p_{3/2}$, thereby blocking the $N = 32$ sub-shell gap. The energy gap between ESPEs of $p_{1/2}$ and $p_{3/2}$ orbitals ($\Delta E_{p_{1/2}, p_{3/2}} = \epsilon_{p_{1/2}} - \epsilon_{p_{3/2}}$) obtained from multipole components ($k = 0, 1$ and 2) of the effective interaction, are shown in Fig. 4(b) for Cr to Ca. The $\Delta E_{p_{1/2}, p_{3/2}}$ value, representing the $N = 32$ sub-shell gap, remains almost constant in the central part while it slightly decreases in $k = 1$ part as one moves from Cr to Ca. But in the $k = 2$ or tensor part, it gradually increases from Cr to Ca, aligning with observations made in Fig. 3. This indicates that the tensor component is solely responsible for establishing the $N = 32$ sub-shell gap. The $N = 34$ sub-shell gaps or $\Delta E_{f_{5/2}, p_{1/2}} = \epsilon_{f_{5/2}} - \epsilon_{p_{1/2}}$, derived from the central, spin-orbit, and tensor components of the effective interaction, are presented in Fig. 4(c). From Fig. 4(c), it can be observed that the $\Delta E_{f_{5/2}, p_{1/2}}$ exhibit similar patterns from Cr to Ca in both central and tensor components as those seen in Fig. 3. This implies that both central and tensor components play crucial roles in the development $N = 34$ sub-shell gap. Notably, the combined effects of central and tensor components have been highlighted in the emergence

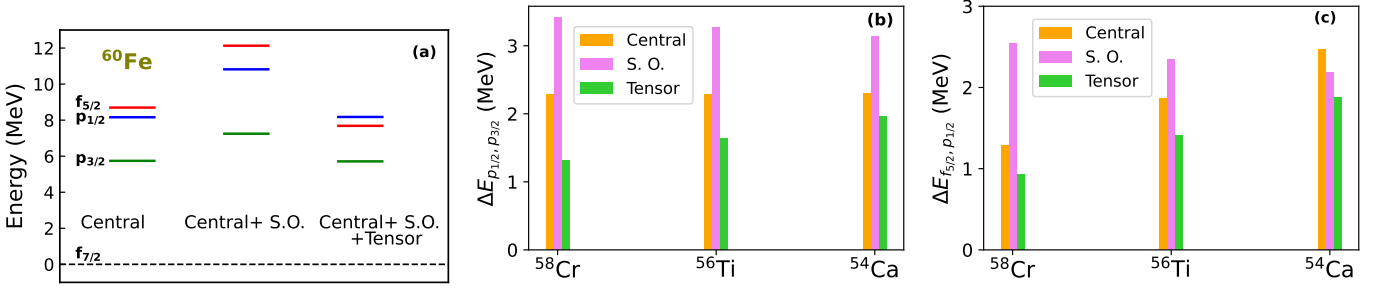


Figure 4: (a): Central, spin-orbit (S. O.) and tensor contribution to neutron ESPEs in ^{60}Fe . (b): Energy gap between ESPEs of $\nu p_{1/2}$ and $\nu p_{3/2}$ orbitals obtained from central, S. O., and tensor parts. (c): Same as (b) but for the energy gap between ESPEs of $\nu f_{5/2}$ and $\nu p_{1/2}$ orbitals.

of $N = 34$ sub-shell closure in the Ca chain as well as in the evolution of $N = 20$ and 28 shell gaps in earlier studies based on phenomenological interactions [2, 23, 24].

When we go below Ca, there is a gradual increase in the $N = 34$ sub-shell gap, while the strength of the $N = 32$ sub-shell gap decreases from Ar to Si. The evolution of neutron ESPEs in ^{52}Ar , ^{50}S and ^{46}Si is displayed through Fig 5. As protons are removed, the ESPEs are shifted upward as a whole, implying that the total proton-neutron monopole interaction is attractive. We observed that the energy gap $\Delta E_{p_{1/2}, p_{3/2}} = 2.40$ MeV in ^{52}Ar , which is nearly similar to that found in ^{58}Cr (~ 2.45 MeV). It further decreases to 2.00 MeV and 0.83 MeV in ^{50}S and ^{46}Si , respectively. This suggests that the $N = 32$ sub-shell gap is rather weak in Ar and disappears in S and Si. In contrast, the strength of $N = 34$ sub-shell gap or $\Delta E_{f_{5/2}, p_{1/2}}$ is 2.53 MeV in ^{52}Ar , comparatively larger than that at ^{54}Ca (~ 2.21 MeV). From Fig 5, we can see that the ESPE of $f_{5/2}$ orbital is slightly positive in ^{50}S and eventually becomes unbound in ^{46}Si by attaining a large positive value. Consequently, the $N = 34$ sub-shell gap, widens further in ^{50}S and ^{46}Si . This leads to a relatively larger $E(2^+)$ value observed in the $N = 34$ isotones (right panel of Fig. 2). The shell model calculations with SDPF-MU interaction also draw a similar conclusion where the $N = 34$ sub-shell gap strengthens below Ca and is extended up to Si [12]. However, in contrast to VS-IMSRG results, the SDPF-MU interaction predicts that for isotopes with $Z < 20$, the strength of the $N = 32$ sub-shell gap has a similar magnitude to that observed in Ca [10, 13].

To visualize the effect of tensor forces, the neutron ESPEs are also calculated without tensor components in Fig. 5. The $f_{5/2}$ orbit remains unbound in the absence of tensor components. On an average, the inclusion of tensor components reduces $\Delta E_{p_{1/2}, p_{3/2}}$ and $\Delta E_{f_{5/2}, p_{1/2}}$ by ~ 1.2 and ~ 2.4 times, respectively. It is quite interesting to see that within the fp -shell, the $N = 32$ sub-shell gap is largely driven by tensor forces; however, the tensor component has a lesser effect on this sub-shell gap below Ca. This can be explained by the nature of tensor forces, as extensively discussed in Refs. [16, 20, 22]. The tensor forces between proton-neutron orbitals ($V_{jj'}^T$) with $\Delta n = 0$ have large spatial overlaps and are stronger than those where $\Delta n \neq 0$ while they tend to vanish when j or $j' = s_{1/2}$. Hence, when we move below Ca, and protons lie within sd -shell, the tensor component has a relatively smaller impact on p - orbitals

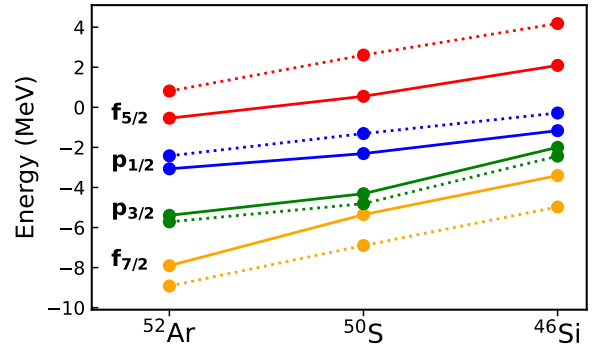


Figure 5: Evolution of neutron ESPEs with (solid lines) and without (dotted lines) tensor forces in nuclei with $Z < 20$.

than f - orbitals. The present study shows that the nature of tensor forces obtained from VS-IMSRG is consistent with those observed from other well-established phenomenological interactions and thus provides a more realistic picture of the impact of tensor forces on the underlying nuclear shell structure.

$N = 32$ isotones: As we have seen above, the $N = 32$ sub-shell effect is weak in isotopes with $Z < 20$. It is worthwhile to discuss the structural characteristics of these isotones adjacent to the $N = 34$ magic number. The low-energy excitation spectra of the $N = 32$ isotones obtained with VS-IMSRG are shown in Fig. 6 alongside the $E2$ transition strengths connecting them. The VS-IMSRG results are found to be in good agreement with the available experimental data in ^{50}Ar and ^{52}Ca . Meanwhile, the *ab initio* results of ^{48}S and ^{46}Si will offer valuable insights into the structure of these exotic isotopes, where experimental data are currently lacking, and will serve as a useful reference for future experiments.

The VS-IMSRG predicts a low-lying 0_2^+ state in ^{50}Ar , ^{48}S and ^{46}Si . The absolute $E2$ transition strengths are always underestimated by VS-IMSRG, primarily due to missing contributions from many-particle, many-hole excitations outside the model space [60]. However, they are successful in qualitatively reproducing the experimental trends [43, 60], and the relative $E2$ strengths are meaningful. Based on the calculated excitation energies and interconnected $B(E2)$ values, two bands are predicted for the $N = 32$ isotones from Ar to Si: a ground-state band connecting the 0_1^+ , 2_1^+ , and 4_1^+ states, and a second band

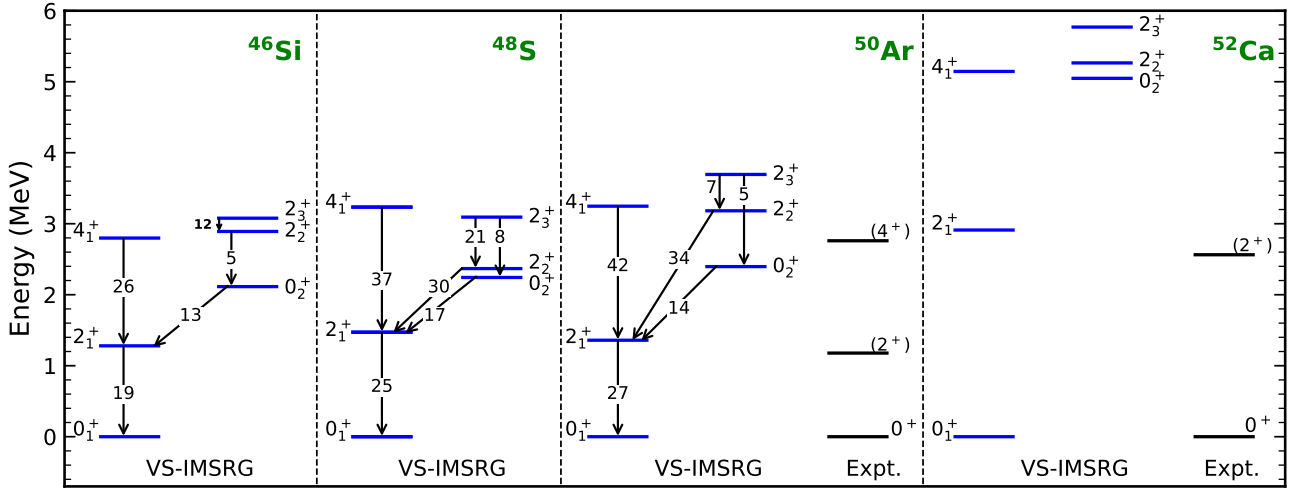


Figure 6: Calculated (blue) and experimental [52] (black) low-lying excitation spectrum and $B(E2)$ values (in $e^2\text{fm}^4$) in $N = 32$ isotones with $Z \leq 20$. All possible $E2$ transitions between low-lying states are considered for which $B(E2)$ is larger than $5 e^2\text{fm}^4$.

at low excitation energy on the top of 0_2^+ state. The second band built upon 0_2^+ state consists of 0_2^+ and 2_3^+ states in ^{50}Ar and ^{48}S while 2_2^+ appears as its band member in ^{46}Si instead of 2_3^+ . Notably, the inter-band $E2$ transitions are not weak, implying configuration mixing in the corresponding wave functions. In contrast, ^{52}Ca exhibits closed shell configuration, as depicted in Fig. 6. The VS-IMSRG results are consistent with the experimental observations and shell model predictions that point towards the onset of collectivity in ^{50}Ar [14] lying beside the $N = 34$ magic number. Moreover, our calculations suggest that this collective behavior further continues in S and Si.

Table 2: Calculated quadrupole moments of the 2^+ states associated with different bands and occupation numbers of the $\nu p_{1/2}$ and $\nu f_{5/2}$ orbitals for 0_1^+ and 0_2^+ states in $N = 32$ isotones.

Nuclei	Q_s ($e \text{ fm}^2$)		$n_\nu[p_{1/2}]$		$n_\nu[f_{5/2}]$	
	2_1^+	2_3^+	0_1^+	0_2^+	0_1^+	0_2^+
^{50}Ar	10.8	1.6	1.005	1.013	0.408	0.456
^{48}S	6.1	-2.5	1.059	0.920	0.637	0.724
^{46}Si	8.5	-1.4 ^a	1.292	0.790	0.657	0.627

^a Corresponds to 2_2^+ instead of 2_3^+ .

The nature of nuclear deformation can be revealed through the spectroscopic quadrupole moments of the 2^+ states ($Q_s(2^+)$) associated with the bands built upon 0_1^+ and 0_2^+ states. The Q_s values of the 2^+ states corresponding to different bands in ^{50}Ar , ^{48}S and ^{46}Si are listed in Table 2. In this case, $Q_s(2^+) = 0$ corresponds to a spherical shape, $Q_s(2^+) > 0$ signifies oblate deformation, and a negative value of Q_s indicates prolate deformation, respectively. The $Q_s(2_2^+)$ or $Q_s(2_3^+)$ values are small lying around zero whereas the $Q_s(2_1^+)$ values are notably larger and positive. This implies that the ground state is oblate deformed and coexists with a nearly spherical or slightly deformed band at low-excitation energy. The neutron occupancies (n_ν) of $p_{1/2}$ and $f_{5/2}$ orbitals ($n_\nu[p_{1/2}]$ and $n_\nu[f_{5/2}]$) for 0_1^+ and 0_2^+ states

are also shown alongside the quadrupole moments in Table 2. These orbitals lie outside the normally filled configuration of $N = 32$ isotones. In the ground states, the total neutron occupancies of these two orbitals are around ~ 1.6 , indicating quenching of the $N = 32$ shell gap and mixing of cross-shell configurations. Such mixing is also predicted in the ground state configurations of ^{50}Ar from shell model calculations with empirical interactions [10, 13, 14]. Further, the $n_\nu[p_{1/2}]$ and $n_\nu[f_{5/2}]$ values are nearly same in 0_1^+ and 0_2^+ states. It suggests that the cross-shell configurations in both states are approximately similar, and hence, the $E2$ transition strength between these two bands remains strong. In contrast, the n_ν values for $p_{1/2}$ and $f_{5/2}$ orbitals are significantly lower, ~ 0.16 , in doubly magic ^{52}Ca . Further, $n_\nu[f_{5/2}]$ is also very small, around 0.7, in ^{52}Ar and ^{50}S , which reflects the prominence of the $N = 34$ shell gap. Earlier, VS-IMSRG calculations have suggested the dominance of cross-shell configurations and deformed ^{42}Si and ^{44}S nuclei at $N = 28$ [39]. As one progresses to more exotic isotopes, the spherical configuration is attained at $N = 34$.

4. Summary

The VS-IMSRG interactions, derived from chiral NN and NNN forces, are employed to study the shell evolution at $N = 32$ and 34 in neutron-rich isotopes with $14 \leq Z \leq 26$. The shell structures are investigated by analyzing $E(2_1^+)$ levels and the evolution of ESPEs. The calculated results are found to be in good agreement with the experimental data. Within fp -shell, the VS-IMSRG results suggest $N = 32$ sub-shell closure in Ca, Ti, which weakens in Cr and gradually disappears in Fe, while the $N = 34$ sub-shell gap emerges exclusively in Ca. Remarkably, this sub-shell closure continues to persist even below Ca, extending as far as Si. The strengthening of the $N = 34$ sub-shell gap is also observed from ESPEs, while the $N = 32$ sub-shell is weak or vanishes below Ca. The effective interactions are then decomposed into multipole components, and their

contributions to the development of shell gaps are addressed through ESPEs. In fp -shell, the $N = 32$ sub-shell closure is primarily driven by the tensor component, whereas both the central and tensor components significantly contribute to the establishment of the $N = 34$ sub-shell gap. The impact of tensor forces on shell gaps is also shown for nuclei with $Z < 20$. Next, we have discussed the low-lying structures of the exotic $N = 32$ isotones for $Z \leq 20$ adjacent to the $N = 34$ magic number. The VS-IMSRG calculations predict the presence of intruder configurations and a deformed ground state band in the ^{50}Ar , ^{48}S , and ^{46}Si isotopes, coexisting with a slightly deformed band at low excitation energy. The *ab initio* results of the present work provide deeper insights into the structure of exotic nuclei, highlighting various components of realistic nuclear forces and their roles in the development of magic numbers far from stability.

Acknowledgements

We are grateful to Takayuki Miyagi for providing the chiral NN and NNN nuclear matrix elements (EM1.8/2.0 interaction), which are generated through the NuHamil code [61]. S.S. would like to thank UGC (University Grant Commission), India, for financial support for his Ph.D. thesis work. P.C.S. acknowledges a research grant from SERB (India), CRG/2022/005167. We are grateful to the National Supercomputing Mission (NSM) for providing computing resources of ‘PARAM Ganga’ at the Indian Institute of Technology Roorkee, implemented by C-DAC and supported by the Ministry of Electronics and Information Technology (MeitY) and Department of Science and Technology (DST), Government of India.

References

- [1] O. Sorlin and M.-G. Porquet, *Prog. Part. Nucl. Phys.* **61**, 602 (2008).
- [2] T. Otsuka, A. Gade, O. Sorlin, T. Suzuki, and Y. Utsuno, *Rev. Mod. Phys.* **92**, 015002 (2020).
- [3] G. Hagen, M. Hjorth-Jensen, G. R. Jansen, R. Machleidt, and T. Papenbrock, *Phys. Rev. Lett.* **109**, 032502 (2012).
- [4] H. Hergert, S. K. Bogner, T. D. Morris, S. Binder, A. Calci, J. Langhammer, and R. Roth, *Phys. Rev. C* **90**, 041302(R) (2014).
- [5] V. Somà, C. Barbieri, T. Duguet, and P. Navrátil, *Eur. Phys. J. A* **57**, 135 (2021).
- [6] D. Steppenbeck *et al.*, *Nature* **502**, 207 (2013).
- [7] X. Xu *et al.*, *Phys. Rev. C* **99**, 064303 (2019).
- [8] E. Leistschneider *et al.*, *Phys. Rev. Lett.* **126**, 042501 (2021).
- [9] S. Iimura *et al.*, *Phys. Rev. Lett.* **130**, 012501 (2023).
- [10] D. Steppenbeck *et al.*, *Phys. Rev. Lett.* **114**, 252501 (2015).
- [11] M. Rosenbusch *et al.*, *Phys. Rev. Lett.* **114**, 202501 (2015).
- [12] H. N. Liu *et al.*, *Phys. Rev. Lett.* **122**, 072502 (2019).
- [13] M. L. Cortés *et al.*, *Phys. Rev. C* **102**, 064320 (2020).
- [14] B. D. Linh *et al.*, *Phys. Rev. C* **109**, 034312 (2024).
- [15] T. Otsuka, R. Fujimoto, Y. Utsuno, B. A. Brown, M. Honma, and T. Mizusaki, *Phys. Rev. Lett.* **87**, 082502 (2001).
- [16] T. Otsuka, T. Suzuki, R. Fujimoto, H. Grawe, and Y. Akaishi, *Phys. Rev. Lett.* **95**, 232502 (2005).
- [17] M. Honma, T. Otsuka, B. A. Brown, and T. Mizusaki, *Phys. Rev. C* **65**, 061301(R) (2002).
- [18] M. Honma, T. Otsuka, B. A. Brown, and T. Mizusaki, *Phys. Rev. C* **69**, 034335 (2004).
- [19] M. Honma, T. Otsuka, B. A. Brown, and T. Mizusaki, *Eur. Phys. J. A* **25**, 499 (2005).
- [20] T. Otsuka, T. Suzuki, M. Honma, Y. Utsuno, N. Tsunoda, K. Tsukiyama, and M. H. Jensen, *Phys. Rev. Lett.* **104**, 012501 (2010).
- [21] B. Bhoj, P. C. Srivastava and K. Kaneko, *J. Phys. G: Nucl. Part. Phys.* **47**, 065105 (2020).
- [22] Y. Utsuno, *Physics* **4**, 185 (2022).
- [23] N. A. Smirnova, B. Bally, K. Heyde, F. Nowacki, K. Sieja, *Phys. Lett. B* **686**, 109 (2010).
- [24] N. A. Smirnova, K. Heyde, B. Bally, F. Nowacki, and K. Sieja, *Phys. Rev. C* **86**, 034314 (2012).
- [25] H. Hergert, S.K. Bogner, T.D. Morris, A. Schwenk, K. Tsukiyama, *Phys. Reports* **621**, 165 (2016).
- [26] S. R. Stroberg, H. Hergert, S. K. Bogner, and J. D. Holt, *Annu. Rev. Nucl. Part. Sci.* **69**, 307 (2019).
- [27] L. Coraggio and N. Itaco, *Front. Phys.* **8**, 345 (2020).
- [28] E. Dikmen, A. F. Lisetskiy, B. R. Barrett, P. Maris, A. M. Shirokov and J. P. Vary, *Phys. Rev. C* **91**, 064301 (2015).
- [29] N. A. Smirnova, B. R. Barrett, Y. Kim, I. J. Shin, A. M. Shirokov, E. Dikmen, P. Maris and J. P. Vary, *Phys. Rev. C* **100**, 054329 (2019).
- [30] G. R. Jansen, J. Engel, G. Hagen, P. Navrátil, and A. Signoracci, *Phys. Rev. Lett.* **113**, 142502 (2014).
- [31] G. R. Jansen, M. D. Schuster, A. Signoracci, G. Hagen, and P. Navrátil, *Phys. Rev. C* **94**, 011301(R) (2016).
- [32] S. K. Bogner, H. Hergert, J. D. Holt, A. Schwenk, S. Binder, A. Calci, J. Langhammer, and R. Roth, *Phys. Rev. Lett.* **113**, 142501 (2014).
- [33] S. R. Stroberg, H. Hergert, J. D. Holt, S. K. Bogner and A. Schwenk, *Phys. Rev. C* **93**, 051301(R) (2016).
- [34] S. R. Stroberg, A. Calci, H. Hergert, J. D. Holt, S. K. Bogner, R. Roth and A. Schwenk, *Phys. Rev. Lett.* **118**, 032502 (2017).
- [35] C. Sarma and P. C. Srivastava, *J. Phys. G* **50**, 045105 (2023).
- [36] S. Sahoo, P. C. Srivastava, and T. Suzuki, *Nucl. Phys. A* **1032**, 122618 (2023).
- [37] B.S. Hu, Z. H. Sun, G. Hagen, G.R. Jansen, T. Papenbrock, *Phys. Lett. B* **858**, 139010 (2024).
- [38] B.S. Hu, Z.H. Sun, G. Hagen, and T. Papenbrock, *Phys. Rev. C* **110**, L011302 (2024).
- [39] Q. Yuan, J.G. Li, and H.H. Li, *Phys. Lett. B* **848**, 138331 (2024).
- [40] Q. Yuan, J. G. Li, and W. Zuo, *Phys. Rev. C* **109**, L041301 (2024).
- [41] Q. Yuan and B.S. Hu, *Phys. Lett. B* **858**, 139018 (2024).
- [42] A. Tichai, K. Kapás, T. Miyagi, M.A. Werner, Ö. Legeza, A. Schwenk, and G. Zarand, *Phys. Lett. B* **855**, 138841 (2024).
- [43] T. Miyagi, S. R. Stroberg, J. D. Holt and N. Shimizu, *Phys. Rev. C* **102**, 034320 (2020).
- [44] J.G. Li, H.H. Li, S. Zhang, Y.M. Xing, and W. Zuo, *Phys. Lett. B* **846**, 138197 (2023).
- [45] K. Hebeler, S. K. Bogner, R. J. Furnstahl, A. Nogga, and A. Schwenk, *Phys. Rev. C* **83**, 031301(R) (2011).
- [46] J. Simonis, K. Hebeler, J. D. Holt, J. Menéndez, and A. Schwenk, *Phys. Rev. C* **93**, 011302(R) (2016).
- [47] T. D. Morris, N. M. Parzuchowski, and S. K. Bogner, *Phys. Rev. C* **92**, 034331 (2015).
- [48] T. Miyagi, S. R. Stroberg, P. Navrátil, K. Hebeler, and J. D. Holt, *Phys. Rev. C* **105**, 014302 (2022).
- [49] S. R. Stroberg, <https://github.com/ragnarstroberg/imsrg>.
- [50] N. Shimizu, T. Mizusaki, Y. Utsuno and Y. Tsunoda, *Comput. Phys. Comm.* **244**, 372 (2019).
- [51] S. R. Stroberg, J. D. Holt, A. Schwenk, and J. Simonis, *Phys. Rev. Lett.* **126**, 022501 (2021).
- [52] Data extracted using the National Nuclear Data Center World Wide Web site from the evaluated nuclear structure data file, <https://www.nndc.bnl.gov/ensdf/>.
- [53] Y. Z. Ma, L. Coraggio, L. De Angelis, T. Fukui, A. Gargano, N. Itaco, and F. R. Xu, *Phys. Rev. C* **100**, 034324 (2019).
- [54] T. Duguet, and G. Hagen, *Phys. Rev. C* **85**, 034330 (2012).
- [55] T. Duguet, H. Hergert, J. D. Holt, and V. Soma, *Phys. Rev. C* **92**, 034313 (2015).
- [56] V. Somà and T. Duguet, *Phil. Trans. R. Soc. A* **382**, 20230117 (2024).
- [57] M. W. Kirson, *Phys. Lett. B* **51**, 110 (1973).
- [58] K. Yoro, *Nucl. Phys. A* **333**, 67 (1980).
- [59] B. A. Brown, W. A. Richter and B. H. Wildenthal, *J. Phys. G* **11**, 1191 (1985).
- [60] S. R. Stroberg, J. Henderson, G. Hackman, P. Ruotsalainen, G. Hagen, and J. D. Holt, *Phys. Rev. C* **105**, 034333 (2022).
- [61] T. Miyagi, *Eur. Phys. J. A* **59**, 150 (2023).